

Self-assembly of hydrogen-bonded two-dimensional quasicrystals

Natalie A. Wasio¹, Rebecca C. Quardokus¹, Ryan P. Forrest¹, Craig S. Lent², Steven A. Corcelli¹, John A. Christie¹, Kenneth W. Henderson¹ & S. Alex Kandel¹

The process of molecular self-assembly on solid surfaces is essentially one of crystallization in two dimensions, and the structures that result depend on the interplay between intermolecular forces and the interaction between adsorbates and the underlying substrate¹. Because a single hydrogen bond typically has an energy between 15 and 35 kilojoules per mole, hydrogen bonding can be a strong driver of molecular assembly; this is apparent from the dominant role of hydrogen bonding in nucleic-acid base pairing, as well as in the secondary structure of proteins. Carboxylic acid functional groups, which provide two hydrogen bonds, are particularly promising and reliable in creating and maintaining surface order, and self-assembled monolayers of benzoic acids produce structure that depends on the number and relative placement of carboxylic acid groups^{2–6}. Here we use scanning tunnelling microscopy to study self-assembled monolayers of ferrocenecarboxylic acid (FcCOOH), and find that, rather than producing dimeric or linear structures typical of carboxylic acids, FcCOOH forms highly unusual cyclic hydrogen-bonded pentamers, which combine with simultaneously formed FcCOOH dimers to form two-dimensional quasicrystallites that exhibit local five-fold symmetry and maintain translational and rotational order (without periodicity) for distances of more than 400 Ångströms.

Quasicrystals—first observed experimentally in 1982—exhibit long-range, non-periodic order, and may contain extended regions with ‘forbidden’ (5, 8, 10 or 12-fold) rotational symmetry^{7,8}. The majority of known quasicrystals are binary or ternary metal alloys such as AlCuMn, or are materials derived from these alloys by adsorption or epitaxy^{9,10}. Apart from metal alloys, other quasicrystalline systems discovered include terpolymer systems¹¹, liquid crystals and micelles^{12,13}, and metal¹⁴ and silica¹⁵ nanoparticle assemblies. FcCOOH, then, represents an entirely new class of quasicrystalline materials, and is the only one in which molecular self-assembly results in five-fold symmetry.

The compound ferroceneacetic acid (FcCH_2COOH) differs from FcCOOH only by the addition of a methylene group between the ferrocene and the carboxylic acid (Fig. 1a) and it shows no evidence of pentamer formation, instead forming monolayers of close-packed dimers. Molecular-resolution images of FcCOOH and FcCH_2COOH monolayers on gold (Au(111)) surfaces acquired using scanning tunnelling microscopy (STM) are presented in Fig. 1b (FcCH_2COOH) and Fig. 1c, d (FcCOOH). The FcCH_2COOH monolayer is ordered and regular, consistent with the formation of doubly hydrogen-bonded dimers, followed by dense packing of these dimers into a lattice. STM resolution of ferrocene groups in covalently bound dimers depends on the relative orientation between the ring system and the surface, with rings parallel to the surface creating much brighter features, and perpendicularly oriented ferrocene much dimmer¹⁶. The presence of both bright and dim features in Fig. 1b shows that FcCH_2COOH , too, has a range of adsorption conformations. Interpretation of the monolayer as consisting of rows of dimers results in an Fe–Fe hydrogen bonding distance of 11.3 Å and an intermolecular spacing of 6.7 Å, consistent with the condensed-phase distances determined crystallographically¹⁷.

The FcCOOH monolayer, however, has no apparent long-range periodicity. Nearly all bright molecular features are grouped into pentagons, though there are some dimers and other defects evident. In addition to areas such as these, where pentamers cover the surface with nearly a complete monolayer, we have also observed areas of the surface with lower adsorbate density; at these lower coverages, isolated pentamers are present (Extended Data Fig. 1a). This result is at odds with the preference for dimer formation observed for monolayers of aliphatic and benzoic carboxylic acids^{3–5}, the structure of the FcCH_2COOH monolayer shown here and the known three-dimensional crystal structure of solid FcCOOH (ref. 17).

Catimers are chains of carboxylic acids in which each molecule hydrogen-bonds to two others; for some acids, catimers constitute either the lowest-energy structure or a metastable structure resulting in lattice polymorphism¹⁸. The degree of hydrogen bonding is the same as for dimer formation, although catimers are generally disfavoured because of non-optimal OH···O bond angles, as well as for entropic reasons. We propose that the FcCOOH pentamers observed are cyclic catimers (Fig. 2b). Cyclization would at first seem to create even more bond strain in OH···O hydrogen bonds, and impose a higher cost in entropy. However, this is offset by an additional favourable interaction between the carbonyl group and the hydrogen atom on the second position of

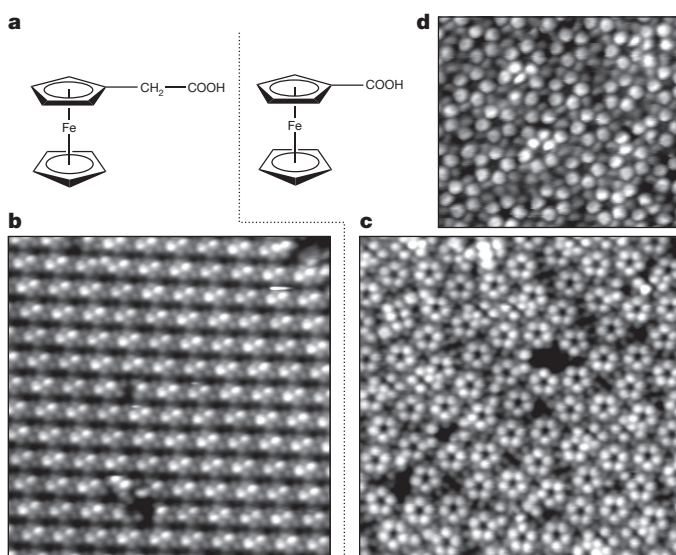


Figure 1 | STM images of FcCOOH and FcCH_2COOH . **a**, Structure of FcCH_2COOH and FcCOOH acid. **b, c**, Rows of dimers are observed for FcCH_2COOH (**b**), whereas the structure of FcCOOH (**c**) is dominated by pentamers; both images are 205 Å × 205 Å. **d**, Higher-resolution, 110 Å × 100 Å image showing submolecular structure in the FcCOOH Cp rings; dimer features packed between pentamers also appear more clearly in this image.

¹Department of Chemistry and Biochemistry, University of Notre Dame, Notre Dame, Indiana 46556, USA. ²Department of Electrical Engineering, University of Notre Dame, Notre Dame, Indiana 46556, USA.

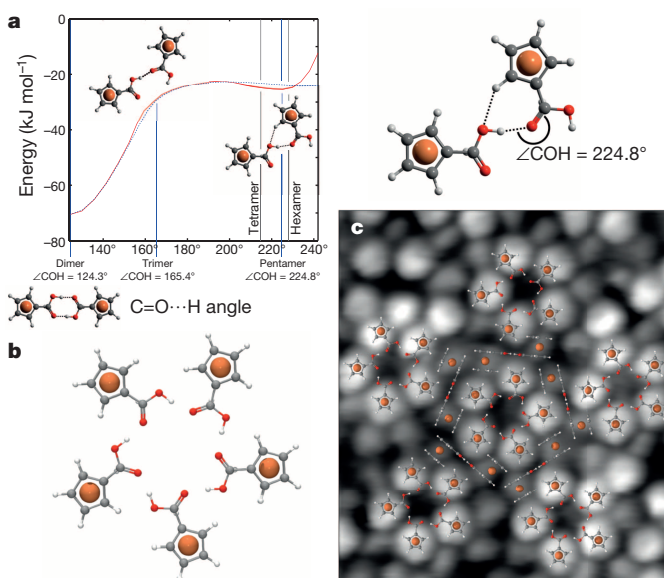


Figure 2 | Calculations and proposed structures for FcCOOH dimers and pentamers. **a**, Calculated energies for FcCOOH dimers as a function of bond angle $\angle\text{COH}$ (red) compared with a similar calculation for HCOOH dimers (blue). Both molecules have the same deep well for the doubly bonded dimer, but only FcCOOH has the additional well at $\angle\text{COH} = 225^\circ$ from $\text{CH}\cdots\text{O}$ hydrogen bonding. Thin vertical lines show the angles necessary for formation of cyclic structures with three to six FcCOOH molecules. **b**, Minimum-energy structure of $(\text{FcCOOH})_5$ calculated by DFT. **c**, Model structure, with the central pentamer surrounded by five FcCOOH dimers; the pentamer has Cp rings parallel to the surface and appears bright in the images, whereas the perpendicular Cp rings of the dimer result in much dimmer features. The model is compared with the image in Fig. 1d, scaled and rotated, and slightly stretched to correct for distortion in the STM image.

the cyclopentadienyl (Cp) ring. Bringing these atoms into proximity allows for the formation of a $\text{CH}\cdots\text{O}$ hydrogen bond. Such bonds are typically less than 10 kJ mol^{-1} in strength, and although they are not generally considered in small-molecule interactions, they are known to influence lattice ordering in crystals, and are important in the structure and function of large biomolecules¹⁹. Although $\text{CH}\cdots\text{O}$ hydrogen bonds are not evident in the crystal structure of FcCOOH, there is evidence that $\text{CH}\cdots\text{N}$ bonding occurs in the solid-state structure of FcCN (ref. 20).

We performed density functional theory (DFT) calculations to determine whether $\text{CH}\cdots\text{O}$ interactions were sufficient to offset the bending of $\text{OH}\cdots\text{O}$ bonds. In the first set of calculations, the geometry of a FcCOOH dimer with two hydrogen bonds was optimized, and the minimum-energy structure found to have a 124.3° angle between the intermolecular hydrogen bond and the C=O bond direction of either carbonyl. The angle $\angle\text{COH}$ was varied to determine its effect on the dimer energy, constraining the dimer to be bent while re-optimizing all other aspects of the geometry. The results are shown in Fig. 2a. The dimer geometry has a deep well resulting from two hydrogen bonds; as the angle increases, one of these bonds is broken and the other strained, with energy increasing until the angle reaches 195° . At this point, the favourable $\text{CH}\cdots\text{O}$ interaction outweighs the cost of further bending the $\text{OH}\cdots\text{O}$ bond, leading to a 2.5 kJ mol^{-1} well at $\angle\text{COH} = 225^\circ$. This closely matches the 224.8° angle necessary to form a cyclic pentamer. Furthermore, the COH bond angles for cyclic tetramers or hexamers are displaced from this energy minimum, which supports the experimentally observed predominance of five-membered rings. We repeated the energy calculations using second-order Møller–Plesset perturbation theory with the DFT-optimized geometry, and found an angular dependence similar to that seen in Fig. 2, including a local minimum at 225° .

The blue dotted line in Fig. 2a shows a similar calculation for formic acid (HCOOH) dimers, with the curve scaled to overlay the FcCOOH dimer curve. The functional forms of these curves are nearly identical between $\angle\text{COH} = 125^\circ$ and 200° , indicating that the underlying processes—the breaking of one hydrogen bond and the bending of the other—are largely independent of the rest of the molecule. The well caused by $\text{CH}\cdots\text{O}$ hydrogen bonding, however, is completely absent for formic acid, because the lone hydrogen on the formic acid carbon is never close enough to an oxygen to participate in any intermolecular interaction.

The $\text{CH}\cdots\text{O}$ well at $\angle\text{COH} = 225^\circ$ in Fig. 2a appears shallow, but this is in part because it is a calculation for a strained dimer rather than for a full cyclic pentamer. The strained dimer makes one $\text{OH}\cdots\text{O}$ hydrogen bond and one $\text{CH}\cdots\text{O}$ bond, but leaves unbonded the C=O on one molecule and the COH on the other. In the cyclic pentamer, all C=O and COH groups participate in hydrogen bonding, potentially doubling the cohesive energy per molecule relative to what is shown in Fig. 2a. To determine more accurately the relative stability of the dimer versus the cyclic catemers, we performed additional DFT calculations to obtain energies and optimized geometries for FcCOOH dimers and for hydrogen-bonded rings containing three to six molecules (Extended Data Table 1). In all cases, the pentamer was found to be more stable than any other cyclic structure; of these, the hexamer was the next most stable. The relative stability of the dimer and pentamer depends on the choice of functionals used for the calculation, with B3LYP and PBE predicting the dimer to be more stable and M06-L and M06-2X favouring the pentamer. The two structures are close enough in energy—less than 2 kJ mol^{-1} for all functionals except M06-2X—that both should be observable given that $k_B T (k_B, \text{Boltzmann's constant}; T, \text{temperature})$ ranges from 0.64 to 2.49 kJ mol^{-1} , depending on the point between preparation (298 K) and imaging (77 K) when the structure becomes kinetically frozen.

For FcCH_2COOH molecules, the length of the additional methylene group prevents any interaction between the carboxyl oxygen and the Cp hydrogens. If other factors—for example steric packing of the ferrocene Cp rings—were responsible for pentamer formation, both FcCOOH and FcCH_2COOH would aggregate into pentamers in a similar fashion. In contrast, the observation of dimers and a complete absence of pentamers for FcCH_2COOH provides strong corroborating evidence that it is the $\text{CH}\cdots\text{O}$ bonds that stabilize FcCOOH pentamers. Other explanations, such as registry to the underlying surface, also do not explain the observations: the Au(111) substrate has hexagonal symmetry, and to the extent that benzene remains on the surface, it packs in a rectangular lattice under our experimental conditions²¹. Furthermore, the isolated pentamers observed in Extended Data Fig. 1a are randomly oriented in two dimensions, which rules out the corrugation of the substrate as a driving cause of pentamer formation.

In addition to pentamers, the FcCOOH monolayer contains a number of other bright features that can be resolved in Fig. 1c, d, including dimers and groups of dimers as well as individual bright features. There is also a large number of less bright features between pentamers, which are very dim in Fig. 1c and clearer in Fig. 1d. As for the dim FcCH_2COOH molecules in Fig. 1b, we interpret these as FcCOOH molecules with Cp rings tilted with respect to the surface. A possible structural model is shown in Fig. 2c: the central pentamer is surrounded by five dimers, which well match the observed dim features. This arrangement creates multiple $\text{CH}\cdots\pi$ interactions, which are known to drive ordering in similar systems²². The dimers thus act as ‘glue’ between adjacent pentamers—whereas the brighter pentamer features seem to align vertex to vertex, the dimers create an effectively larger pentagonal unit that then packs edge to edge with its neighbours.

We note that the molecular arrangement in Fig. 1c seems to have a single chirality; the effect is subtle but consistent, and the chirality reverses for the area imaged in Fig. 1d. For neighbouring pentamers aligned vertex to vertex, the two pentagons are offset so that the pair has point symmetry but not plane symmetry; that is, the pentagons’ symmetry

axes may be parallel but not collinear. This observation is explained in the model, because the *trans*-configuration of the dimers in the model in Fig. 2c create handedness that will propagate to create long-range chirality in the monolayer. In some cases, monolayer defects create grain boundaries that interrupt the long-range structure. Both orientation and chirality can change across these boundaries; an example is shown in Extended Data Fig. 5, along with diagrams to illustrate the chiral structure.

The packing of pentamers to form a FcCOOH monolayer results in quasicrystalline structure, which is analysed in Fig. 3. In Fig. 3a, a $405\text{ \AA} \times 360\text{ \AA}$ image of a FcCOOH monolayer is low-pass-filtered to de-emphasize the internal structure of the pentamers and thus emphasize the longer-range order (the raw data are presented in Extended Data Fig. 5d). Each pentamer is then overlaid with a pentagon that—relative to the pentagon formed with molecules at vertices—was expanded in size and rotated by 180° . The image is patterned but has no apparent periodicity, and the pentagons and their interstitial spaces match the shapes in a Penrose ‘P1’ tiling²³ (pentagon, rhombus, boat and star), with only a few small gaps in evidence. A number of intermediate-range structures exactly mirror those of a Penrose tiling, which is drawn in Fig. 3b for comparison. As in the Penrose tiling, orientational ordering of pentagons in the experimental image is nearly perfect, with only two directions observed; this is also presented quantitatively in Extended Data Figs 1b and 2.

Local five-fold and ten-fold symmetry of the FcCOOH monolayer can be seen in the two-dimensional Fourier transform in Fig. 3c and the two-dimensional spatial correlation function in Fig. 3d; the data set used to produce both of these is in Extended Data Fig. 1b. The Fourier transform (Extended Data Fig. 3a) has ten-fold-symmetric peaks at a number of radii, and both the sharpness and the symmetry are characteristic of quasicrystalline ordering. The spatial correlation function (Extended Data Fig. 3b) maps displacement vectors between every pair of pentagons in an image; it, too, shows ten-fold symmetry as well as long-range translational order. This order is quasiperiodic, however, because it corresponds to a sum of multiple frequencies related by irrational ratios: in this case, powers of the golden ratio, $\varphi = (1 + \sqrt{5})/2$ (Extended Data Fig. 4). Quasiperiodicity and orientational order can be considered the essential properties of quasicrystals²⁴. FcCOOH

monolayers are also quasicrystalline by an alternative definition, which requires an essentially sharp diffraction pattern and the absence of translational periodicity²⁵. The relatively small size of ordered regions ($>400\text{ \AA}$) is fairly typical for self-assembled monolayers with hexagonal or other allowed symmetry. FcCOOH might be more accurately described, therefore, as polyquasicrystalline, and the regions imaged here, as quasicrystallites; this is largely a matter of terminology, however.

Differences between the Penrose tiling and the FcCOOH monolayer include the small gaps described above and the presence of relatively more rhombuses and fewer stars, as well as the prevalence of pentagons with four other pentagons immediately adjacent. In a Penrose tiling, pentagons may have two, three or five immediate neighbours, and two adjacent pentagons cannot have the same number of neighbours. Replicating these constraints would be difficult with pairwise interactions, and this probably explains differences between the monolayer and Penrose structures. However, the intermediate-range order of the monolayer matches that of the Penrose tiling quite well.

Maximal packing cannot be the sole driving force in the formation of a quasicrystalline monolayer. Higher-density packing of pentagons is possible with periodic lattices; indeed, other investigations of the self-assembly of molecules with C_5 symmetry uniformly have found monolayers with periodic lattice structures^{26,27}, including a complex (but still periodic) Archimedean tiling²⁸. Random packing of pentagons with the constraint that edges and vertices must match, however, produces patterns that appear much more like quasicrystals²⁹. The structures in ref. 29 are more dendritic and less dense than those we observe for FcCOOH. Physically, we would expect thermal motions during deposition to allow for some reorientation, increasing the packing density until the overall structure either reaches a free-energy minimum or becomes kinetically locked. The result is similar to that predicted when a Metropolis algorithm is used to anneal structure after random growth³⁰.

The spontaneous pentamer formation observed for FcCOOH will probably also occur for molecules functionalized at the 3 and 4 positions—that is, not immediately adjacent to the COOH group; some functionalizations of the other Cp ring may also not hinder pentamer formation. There is potentially a large range of novel supramolecular assemblies based on these pentameric building blocks, in which the chemistry of side groups can control the interaction of pentamers and influence the formation of crystalline or quasicrystalline structure.

METHODS SUMMARY

Solutions of approximately 10 mM of FcCOOH and FcCH₂COOH acid were prepared in an Ar-purged glovebox, using benzene as the solvent. Small quantities of the ferrocene derivatives were loaded into a pulsed solenoid valve and deposited in vacuum onto an Ar-sputtered and annealed Au(111)-on-mica sample at room temperature ($\sim 295\text{ K}$). Once deposited, the sample was immediately transferred into an ultrahigh-vacuum chamber (10^{-10} Torr) at 77 K, and STM images were acquired under constant-current conditions. Image filtering (high pass in the scan direction, or low pass overall) was done in some cases to decrease noise, but no other frequency-selective filter was used. DFT calculations were performed using the Q-CHEM software package³¹. The 6-311+G** basis set was used for all C, H and O atoms, and the LANL2TZ effective core potential basis set was used for all Fe atoms.

Online Content Any additional Methods, Extended Data display items and Source Data are available in the online version of the paper; references unique to these sections appear only in the online paper.

Received 1 August; accepted 12 December 2013.

- Smith, R., Lewis, P. & Weiss, P. Patterning self-assembled monolayers. *Prog. Surf. Sci.* **75**, 1–68 (2004).
- Lackinger, M. & Heckl, W. Carboxylic acids: versatile building blocks and mediators for two-dimensional supramolecular self-assembly. *Langmuir* **25**, 11307–11321 (2009).
- Clair, S. et al. STM study of terephthalic acid self-assembly on Au(111): hydrogen-bonded sheets on an inhomogeneous substrate. *J. Phys. Chem. B* **108**, 14585–14590 (2004).
- Fuhr, J. D. et al. Interplay between hydrogen bonding and molecule–substrate interactions in the case of terephthalic acid molecules on Cu(001) surfaces. *J. Phys. Chem. C* **117**, 1287–1296 (2013).

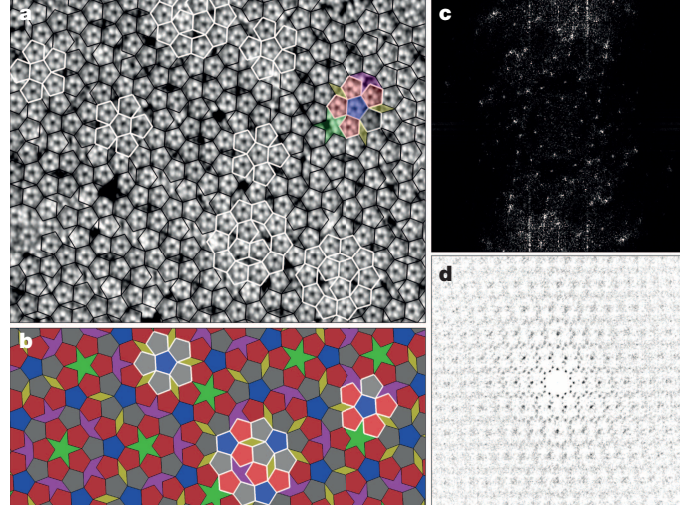


Figure 3 | Comparison of a FcCOOH monolayer structure to a P1 Penrose tiling. **a**, $405\text{ \AA} \times 360\text{ \AA}$ image, overlaid with pentagons to show the long-range, quasicrystalline order. **b**, Groups of pentagons highlighted in white in **a** show some structural motifs common to both the experimental data and a Penrose P1 tiling; the interstitial spaces between pentamers in **a** also match the star, boat and rhombus of the P1 tiling. **c**, Two-dimensional Fourier transform; the innermost ring arises from long-range five-fold and ten-fold symmetry. **d**, This symmetry can also be seen in the two-dimensional spatial correlation function.

5. Heininger, C., Kampschulte, L., Heckl, W. & Lackinger, M. Distinct differences in self-assembly of aromatic linear dicarboxylic acids. *Langmuir* **25**, 968–972 (2009).
6. Ye, Y. et al. A unified model: self-assembly of trimesic acid on gold. *J. Phys. Chem. C* **111**, 10138–10141 (2007).
7. Levine, D. & Steinhardt, P. Quasicrystals—a new class of ordered structures. *Phys. Rev. Lett.* **53**, 2477–2480 (1984).
8. Shechtman, D., Blech, I., Gratias, D. & Cahn, J. Metallic phase with long-range orientational order and no translational symmetry. *Phys. Rev. Lett.* **53**, 1951–1953 (1984).
9. Smerdon, J. A. et al. Nucleation and growth of a quasicrystalline monolayer: bi adsorption on the fivefold surface of i-Al(70)Pd(21)Mn(9). *Phys. Rev. B* **78**, 075407 (2008).
10. Gierer, M. et al. Fivefold surface of quasicrystalline AlPdMn: structure determination using low-energy-electron diffraction. *Phys. Rev. B* **57**, 7628–7641 (1998).
11. Hayashida, K., Dotera, T., Takano, A. & Matsushita, Y. Polymeric quasicrystal: mesoscopic quasicrystalline tiling in ABC star polymers. *Phys. Rev. Lett.* **98**, 195502 (2007).
12. Fischer, S. et al. Colloidal quasicrystals with 12-fold and 18-fold diffraction symmetry. *Proc. Natl Acad. Sci. USA* **108**, 1810–1814 (2011).
13. Zeng, X. et al. Supramolecular dendritic liquid quasicrystals. *Nature* **428**, 157–160 (2004).
14. Talapin, D. V. et al. Quasicrystalline order in self-assembled binary nanoparticle superlattices. *Nature* **461**, 964–967 (2009).
15. Xiao, C., Fujita, N., Miyasaka, K., Sakamoto, Y. & Terasaki, O. Dodecagonal tiling in mesoporous silica. *Nature* **487**, 349–353 (2012).
16. Zhong, D. et al. Multilevel supramolecular architectures self-assembled on metal surfaces. *ACS Nano* **4**, 1997–2002 (2010).
17. Cotton, F. & Reid, A. Solid-state structure of ferrocenecarboxylic acid, [Fe(C₅H₄CO₂H)(C₅H₅)]. *Acta Crystallogr. C* **41**, 686–688 (1985).
18. Beyer, T. & Price, S. Dimer or catemer? Low-energy crystal packings for small carboxylic acids. *J. Phys. Chem. B* **104**, 2647–2655 (2000).
19. Steiner, T. & Desiraju, G. Distinction between the weak hydrogen bond and the van der Waals interaction. *Chem. Commun.* 891–892 (1998).
20. Bell, W., Ferguson, G. & Glidewell, C. Cyanoferrocene: a two-dimensional network generated by short C-H···N hydrogen bonds. *Acta Crystallogr. C* **52**, 1928–1930 (1996).
21. Quardokus, R. et al. Adsorption of diferroenylacetylene on Au(111) studied by scanning tunneling microscopy. *Phys. Chem. Chem. Phys.* **15**, 6973–6981 (2013).
22. Nishio, M. The CH/π hydrogen bond in chemistry. Conformation, supramolecules, optical resolution and interactions involving carbohydrates. *Phys. Chem. Chem. Phys.* **13**, 13873–13900 (2011).
23. Penrose, R. Pentaplexity: a class of non-periodic tilings of the plane. *Eureka* **39**, 16–32 (1978).
24. Levine, D. & Steinhardt, P. Quasi-crystals: 1. Definition and structure. *Phys. Rev. B* **34**, 596–616 (1986).
25. International Union of Crystallography. Report of the Executive Committee for 1991. *Acta Crystallogr. A* **6**, 922–946 (1992).
26. Bauer, T. et al. Building 2D crystals from 5-fold-symmetric molecules. *J. Am. Chem. Soc.* **131**, 3460–3461 (2009).
27. Guillermet, O. et al. Self-assembly of fivefold-symmetric molecules on a threefold-symmetric surface. *Angew. Chem. Int. Ed.* **48**, 1970–1973 (2009).
28. Ecija, D. et al. Five-vertex Archimedean surface tessellation by lanthanide-directed molecular self-assembly. *Proc. Natl Acad. Sci. USA* **110**, 6678–6681 (2013).
29. Bauer, K. & Krey, U. Model-calculations on random pentagon clusters compared to 2D-quasicrystals. *Z. Phys. B* **75**, 385–392 (1989).
30. Reichert, M. & Gahler, F. Cluster model of decagonal tilings. *Phys. Rev. B* **68**, 214202 (2003).
31. Shao, Y. et al. Advances in methods and algorithms in a modern quantum chemistry program package. *Phys. Chem. Chem. Phys.* **8**, 3172–3191 (2006).

Acknowledgements This work was supported by the US National Science Foundation under grant NSF CHE-1124762. The authors acknowledge high-performance computing resources and support from the Center for Research Computing at the University of Notre Dame.

Author Contributions N.A.W. and R.C.Q. performed STM measurements and made the initial experimental discovery. R.P.F., C.S.L. and S.A.C. designed the computational approach, and R.P.F. performed the calculations. J.A.C. and K.W.H. provided the molecules used, as well as several others used as tests and controls. All authors participated in analysis and interpretation of the results. N.A.W. drafted the manuscript. S.A.K. prepared extended data figures, edited the manuscript and coordinated the efforts of the research team.

Author Information Reprints and permissions information is available at www.nature.com/reprints. The authors declare no competing financial interests. Readers are welcome to comment on the online version of the paper. Correspondence and requests for materials should be addressed to S.A.K. (skandel@nd.edu).

METHODS

The synthesis of ferrocenecarboxylic acid follows a modified literature procedure³². All manipulations were carried out using standard Schlenk techniques under a nitrogen (N_2) atmosphere. Reagents and solvents were used as received, with the exception of THF, which was purified by passage through a solvent purification system (Innovative Technology). A flame-dried 100-ml Schlenk flask was charged with ferrocene (1 g, 5.4 mmol), potassium *t*-butoxide (0.075 g, 0.067 mmol) and THF (50 ml). The resulting solution was cooled in a dry-ice acetone bath. A pentane solution of *t*-BuLi (6.33 ml, 1.7 M, 10.8 mmol) was added dropwise via syringe to the vigorously stirred solution over the course of 10 min, during which the solution took on a brighter orange, cloudy appearance. After the solution was allowed to stir for an additional hour at -78°C , CO_2 was bubbled via syringe through the solution for an additional hour, during which the solution became bright yellow and less cloudy. The solution was then allowed to warm to room temperature ($\sim 295\text{ K}$) and quenched with water (20 ml). The reaction was poured onto 100 ml of water and the aqueous phase was washed twice with dichloromethane to extract any unreacted ferrocene. The aqueous phase was separated and acidified with 6 M HCl, followed by extraction with dichloromethane. The organic phase was dried over MgSO_4 and evaporated to give 0.96 g of pure ferrocenecarboxylic acid (77% yield). NMR spectra were recorded on a Bruker-500 spectrometer at 293 K and were referenced internally to the residual signals of the deuterated solvent. ^1H NMR (CDCl_3) δ 4.87 (t, 2H), 4.47 (t, 2H), 4.26 (s, 5H). ^1H NMR (C_6D_6) δ 4.86 (t, 2H), 4.0 (t, 2H), 3.96 (s, 5H).

Solutions of approximately 10 mM of ferrocenecarboxylic acid ($\text{C}_5\text{H}_5\text{FeC}_5\text{H}_4\text{COOH}$) and ferroceneacetic acid ($\text{C}_5\text{H}_5\text{FeC}_5\text{H}_4\text{CH}_2\text{COOH}$, Sigma, 98%) were prepared in an Ar-purged glove-box, using benzene as the solvent. Small quantities of the ferrocene derivatives were loaded into a pulsed solenoid valve and deposited in vacuum onto an Ar-sputtered and annealed Au(111)-on-mica sample at room temperature. Once deposited, the sample was immediately transferred into an ultrahigh-vacuum chamber (10^{-10} Torr) at 77 K.

STM images were acquired at constant current using a mechanically cut Pt-Ir tip. The sample biases and tunnelling currents for the images in the main text were respectively -1.5 V and 5 pA (Fig. 1b), $+1.0\text{ V}$ and 10 pA (Fig. 1c), and $+0.5\text{ V}$ and 10 pA (Figs 1d and 3a).

Image processing for STM data included a low-pass filter (Fig. 3a) or high-pass filtering in the fast-scan direction (Fig. 2 and Extended Data Fig. 5a–c); images in Fig. 1 and Extended Data Fig. 5d show raw instrumental data, adjusted for contrast. Overlapping the data and model in Fig. 2c required stretching the image in the vertical direction to compensate for distortion caused by experimental drift; a similar process was used to correct the data before deriving the correlation functions in Fig. 3d and Extended Data Fig. 3. We note that the effects of image distortion will be minimal for Extended Data Fig. 4, because the one-dimensional section was extracted nearly along the STM's fast-scan direction.

Translational and orientational correlation functions were calculated on the basis of the positions of FcCOOH pentamers. The location of the centre of each pentamer was selected manually, and then each position re-examined carefully using expanded images; the estimated error is one or two pixels, and should not be

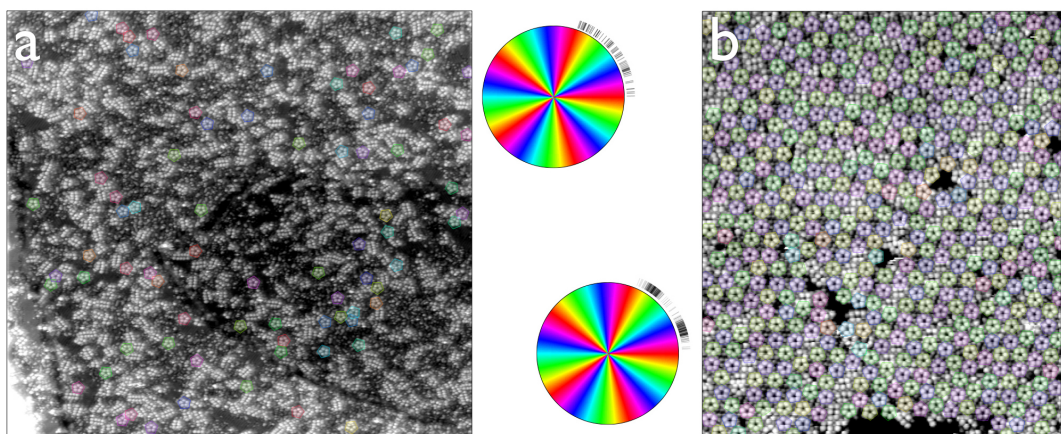
systematically biased. The orientation of each pentamer was calculated automatically by fitting $\sin 5\theta$ and $\cos 5\theta$ functions in the neighbourhood of each pentamer centre. (θ is the angle of any given pixel with respect to the pentamer centre.)

Reliable descriptions of hydrogen-bonded systems often require computationally costly methods such as coupled-cluster theory with singles, doubles and perturbative triples. The complexity of the cyclic catemers makes DFT a better alternative because it is considerably less demanding and provides reasonably accurate results. Because the accuracy of DFT depends sensitively on the functional used to describe electronic exchange and correlation, great care was taken to choose functionals for our calculations that offered a balance between performance and quality. In the limit of the generalized gradient approximation, the more commonly used BLYP functional and B3LYP hybrid-functional do not generally perform well for hydrogen bonding^{33–36}. For this reason calculations were also done using the Perdew–Burke–Ernzerhof (PBE) functional, in particular because of its relative accuracy for $\text{OH}\cdots\text{O}$ hydrogen bonding^{33,34}. Comparable accuracy for $\text{OH}\cdots\text{O}$ hydrogen bonding has also been reported for the M06-2X and M06-L functionals³⁴. Calculations were repeated with all four functionals (B3LYP, PBE, M06-2X and M06-L) to determine whether the qualitative conclusion was dependent on the details of the calculation.

The 6-311++G** basis set was used for all C, H and O atoms, and the LANL2TZ effective core potential basis set was used for all Fe atoms. Each calculation used a Lebedev grid containing 302 angular points with 100 radial shells to reduce numerical integration inaccuracies. To reduce basis-set superposition error, the Boys–Bernardi counterpoise correction method was used for each energy calculation³⁷. All calculations were performed using the Q-CHEM software package³¹.

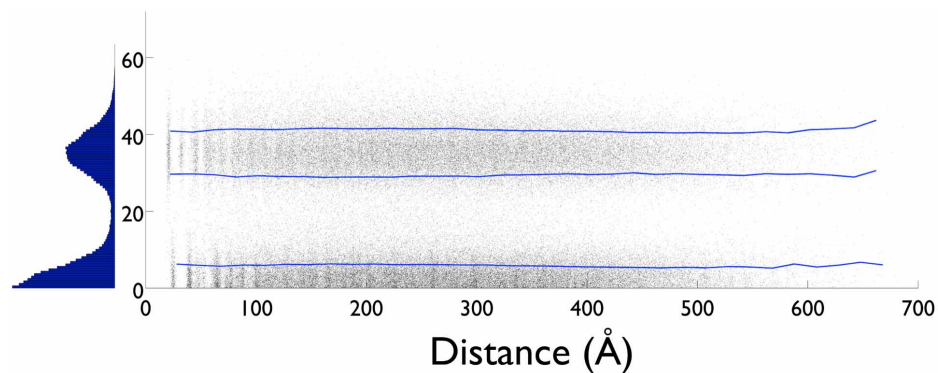
For the bent-dimer optimizations, the dimer bond angle $\angle\text{COH}$ was increased in 5° increments and the geometry was relaxed, with the C and O atoms of each CpCOOH ring restricted to movement within a two-dimensional plane to approximate the effect of being bound to a surface. The same coplanarity constraint was applied for calculation of the cyclic oligomers, which were also forced to maintain the appropriate C_n symmetry.

32. Sanders, R. & Mueller-Westerhoff, U. The lithiation of ferrocene and ruthenocene: a retraction and an improvement. *J. Organomet. Chem.* **512**, 219–224 (1996).
33. Ireta, J., Neugebauer, J. & Scheffler, M. On the accuracy of DFT for describing hydrogen bonds: dependence on the bond directionality. *J. Phys. Chem. A* **108**, 5692–5698 (2004).
34. Thanthiriwatte, K. S., Hohenstein, E. G., Burns, L. A. & Sherrill, C. D. Assessment of the performance of DFT and DFT-D methods for describing distance dependence of hydrogen-bonded interactions. *J. Chem. Theory Comput.* **7**, 88–96 (2011).
35. Tsuzuki, S. & Luthi, H. Interaction energies of van der Waals and hydrogen bonded systems calculated using density functional theory: assessing the PW91 model. *J. Chem. Phys.* **114**, 3949–3957 (2001).
36. Vargas, R., Garza, J., Dixon, D. & Hay, B. How strong is the $\text{C-H}\cdots\text{O}=\text{C}$ hydrogen bond? *J. Am. Chem. Soc.* **122**, 4750–4755 (2000).
37. Boys, S. & Bernardi, F. Calculation of small molecular interactions by differences of separate total energies—some procedures with reduced errors. *Mol. Phys.* **19**, 553–566 (1970).



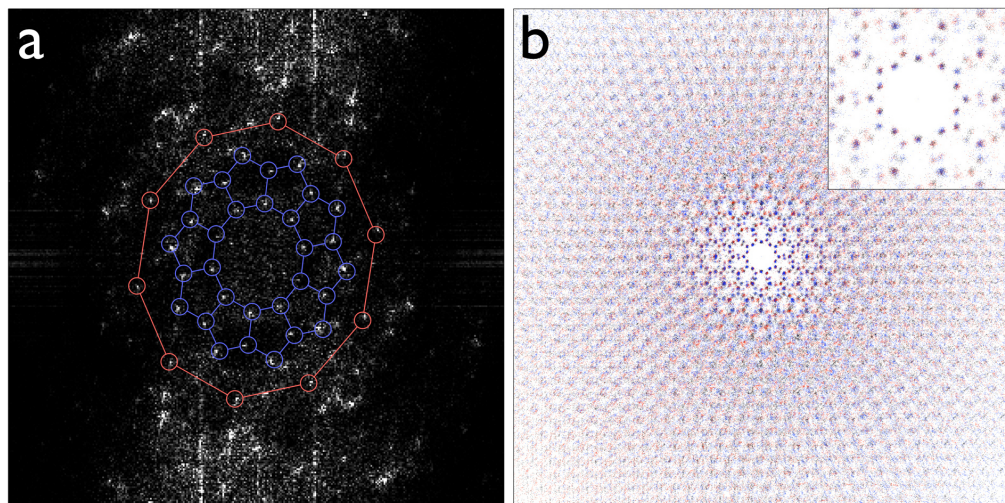
Extended Data Figure 1 | Images of isolated and densely packed pentamers, and measured orientational distributions. **a**, $915 \text{ \AA} \times 860 \text{ \AA}$ image of FcCOOH adsorbed at lower density. Molecules are dispersed over the surface in a wide variety of structures, including two-row rectangular features that may correspond to FcCOOH dimers. Isolated pentamers are evident and are outlined using pentagons, with colour indicating the direction of each

pentamer's symmetry axes, as shown in the colour wheel at the upper right. Tick marks around the colour wheel's circumference show the in-plane orientation of each pentamer, and the distribution of angles is indistinguishable from random. **b**, $470 \text{ \AA} \times 555 \text{ \AA}$ image of FcCOOH at near-complete coverage. Orientations of the pentamers are strongly peaked around two angles.



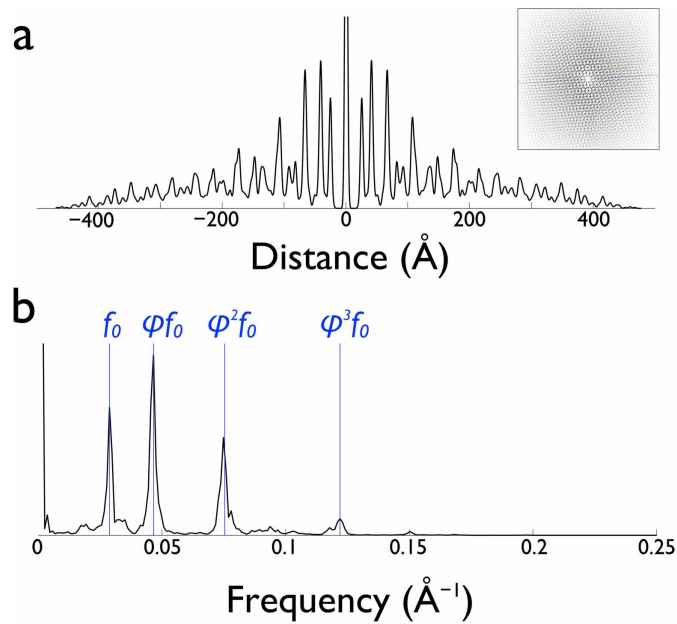
Extended Data Figure 2 | Pentamer-to-pentamer orientational correlation function. Correlation function for pentamer orientations for the image in Extended Data Fig. 1b, once again showing that pentamer orientation is strongly peaked around two angles, but also that the orientational order is

constant over the entire area imaged. Blue lines mark the standard deviation, σ , as a function of distance between pentamer centres. Integrating over all distances produces the histogram shown at the left.

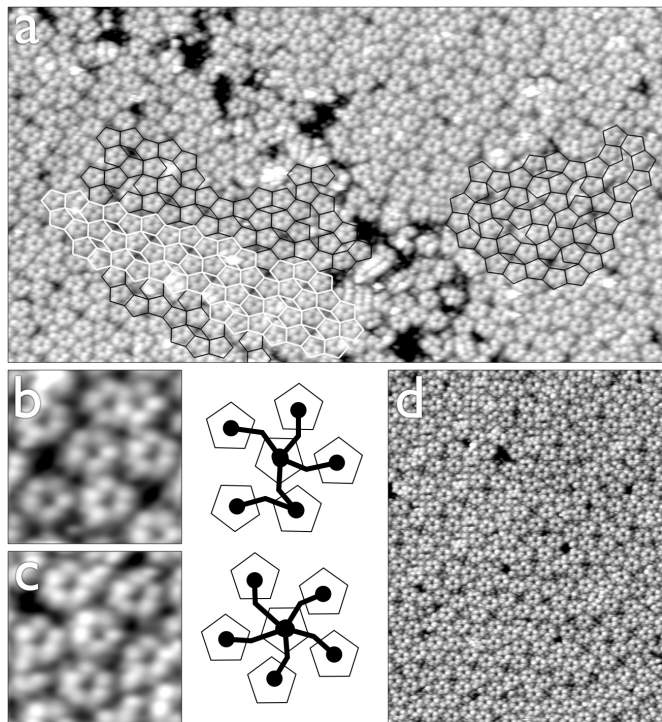


Extended Data Figure 3 | Two-dimensional Fourier transform and two-dimensional spatial correlation function showing five- and ten-fold symmetry of FcCOOH monolayers. **a**, Expanded version of the two-dimensional FFT from Fig. 3c, with overlaid polygons in red and blue showing five- and ten-fold symmetry. Data were low-pass-filtered to remove the d.c. signal and to enhance the contrast of sharp features. **b**, Two-dimensional spatial

correlation function from Fig. 3d, displayed to longer distances to show the persistence of translational order. Red, blue, and black patterns are overlaid, and are based on identical data, except the red and blue point sets are rotated $\pm 36^\circ$; the overlap of all three colours demonstrates the long-range ten-fold symmetry of the data.



Extended Data Figure 4 | Section of the two-dimensional spatial correlation function, with frequency analysis. **a**, Line section of the spatial correlation function from Fig. 3d and Extended Data Fig. 3b (also inset), showing translational order over the entire observed range of over 400 Å. **b**, Fourier transform of **a**. The frequency f_0 corresponds to periodicity with a wavelength of 34.7 Å. Additional frequencies are equal to f_0 times powers of the golden ratio, $\varphi = (1 + \sqrt{5})/2$. The combination of frequencies with irrational ratios is characteristic of quasiperiodic order.



Extended Data Figure 5 | Two adjacent FcCOOH monolayer domains, showing periodic and aperiodic packing as well as a change in overall chirality. **a**, $675 \text{ \AA} \times 365 \text{ \AA}$ image of FcCOOH showing two packed domains with a grain boundary down the centre of the image. The domain at the left of the image has an extended region where pentagons are packed in a periodic (crystalline) fashion, whereas the domain at the right appears quasicrystalline. **b, c**, The orientation of the pentagons differs between the two domains, as does the chirality; **b** is taken from the left-hand side of **a** and **c** is taken from the right-hand side of **a**. **d**, Raw data for Fig. 3, unfiltered and without overlaid pentagons.

Extended Data Table 1 | Calculated energies for FcCOOH clusters, from dimers to hexamers

Cohesive Energy per Molecule (kJ/mol)

	PBE	B3LYP	M06-2X	M06-L
(FcCOOH) ₂	-37.63	-32.96	-37.21	-36.50
(FcCOOH) ₃	-32.13	-30.76	-6.24	-32.03
(FcCOOH) ₄	-33.76	-30.20	-38.00	-34.64
(FcCOOH) ₅	-36.01	-31.29	-41.07	-37.07
(FcCOOH) ₆	-34.32	-29.04	-39.88	-35.96

Geometries for each cluster were optimized subject to the constraint of C_2 to C_6 symmetry. An additional constraint to approximate the effect of surface adsorption was to constrain every CpCOOH ring (C and O atoms) in each oligomer to be coplanar. For each functional, the lowest-energy structure is highlighted in blue, and the second-lowest, in grey.